European Journal of Pharmaceutics and Biopharmaceutics xxx (xxxx) 1–11

Contents lists available at ScienceDirect

European Journal of Pharmaceutics and Biopharmaceutics

journal homepage: www.elsevier.com/locate/ejpb

Research paper

# Solid-state properties of Nifurtimox. Preparation, analytical characterization, and stability of an amorphous phase

Aldana B. Moroni [a], Elena Perez Mayoral [b], Diego F. Lionello [c], Daniel R. Vega [d], Teodoro S. Kaufman [a,*], Natalia.L. Calvo [a,*]

[a] Área de Análisis de Medicamentos, Facultad de Ciencias Bioquímicas y Farmacéuticas, Universidad Nacional de Rosario e Instituto de Química Rosario (IQUIR, CONICET-UNR), Suipacha 531, Rosario S2002LRK, Argentina

[b] Departamento de Química Inorgánica y Química Técnica, Universidad Nacional de Educación a Distancia, UNED, Urbanización Monte Rozas, Avenida Esparta s/n, Ctra. de Las Rozas al Escorial Km 5, 28232 Las Rozas-Madrid, Spain

[c] Departamento Física de la Materia Condensada, Gerencia de Investigación y Aplicaciones, Centro Atómico Constituyentes, Comisión Nacional de Energía Atómica e Instituto Jorge A. Sabato, Universidad Nacional General San Martín, Av. Gral. Paz 1499, B1650KNA, San Martín, Buenos Aires, Argentina

[d] Departamento Física de la Materia Condensada, Gerencia de Investigación y Aplicaciones, Centro Atómico Constituyentes, Comisión Nacional de Energía Atómica y Escuela de Ciencia y Tecnología, Universidad Nacional General San Martín, Av. Gral. Paz 1499, B1650KNA, San Martín, Buenos Aires, Argentina

ARTICLE INFO

*Keywords:*
Amorphous phase
Chemometrics method
Nifurtimox physical phase stability
Solid-state characterization
Spectroscopy and diffractometry
Thermal methods

ABSTRACT

Nifurtimox (NFX) is a nitrofuran derivative used to treat Chagas disease, a neglected disease caused by the protozoan *Trypanosoma cruzi*. The drug is very sparingly soluble in aqueous media and no other solid phases of NFX have been reported to date.

The preparation of the amorphous mode of NFX is reported, as well as its characterization by hot stage microscopy, thermal (differential scanning calorimetry and thermogravimetric analysis), spectroscopic (solid state nuclear magnetic resonance, mid-infrared, and near-infrared), diffractometric and functional (powder dissolution rate) means.

The stability of the new phase was investigated. This was characterized using thermal, spectroscopic, and diffractometric methods, finding out its spontaneous reversion to the crystalline state, as sign of instability. In addition, the amorphous material proved to be sensitive to temperature, pressure, and mechanical stress, all of which accelerated phase conversion. However, it was able to remain stable in a model polymeric amorphous solid dispersion with PEG 4000 for more than one month. An approach for monitoring the conversion of the amorphous phase to its crystalline counterpart under thermal stress by chemometric analysis of mid-infrared spectra at different temperatures is also disclosed.

## 1. Introduction

Nifurtimox (NFX) is 4-[(5-nitrofurfurylidene)amino]l-3-methylthiomorpholine-1,1-dioxide (Fig. S1). The compound is a nitrofuran hydrazone, which became the first drug designed to treat trypanosomiases (sleeping sickness and Chagas disease) [1,2], and was included in the World Health Organization Model List of Essential Medicines [3] in 2009. To date, NFX remains as one of the only two available pharmacological alternatives for treating Chagas disease [4,5], a potentially life-threatening neglected tropical disease [6], that currently affects over 18 million people and is becoming an emergent serious health condition in non-endemic countries [7]. With the aim of drug repurposing, NFX has been patented to treat cancer and inhibit angiogenesis [8] and its potential use against pediatric tumors is under evaluation [9].

The drug has a CLogP lipophilicity value of 0.02 [10], and its aqueous solubility was estimated in the range of 50–100 μg $ml^{-1}$ [11], being considered "practically insoluble in water" [12,13]. NFX belongs to Class II [14,15] in the Biopharmaceutical Classification System (BCS) however, perhaps due to incomplete knowledge of its properties, it has also been graded as BCS IV [16]. In both cases, drug solubility and dissolution rate limit its absorption.

Elguero *et al.* provided the first structural insights into NFX [17], by studying its solution $^{1}H$ and $^{13}C$ nuclear magnetic resonance (NMR) spectra and performing a single crystal X-ray diffraction analysis. In the latter case, they found that the solid exhibited two crystallographically

* Corresponding authors.
*E-mail addresses:* kaufman@iquir-conicet.gov.ar (T.S. Kaufman), calvo@iquir-conicet.gov.ar (Natalia.L. Calvo).

https://doi.org/10.1016/j.ejpb.2023.01.008
Received 19 October 2022; Received in revised form 13 January 2023; Accepted 13 January 2023
0939-6411/© 20XX

independent molecules in the unit cell with slightly different geometries, and that the thiazide ring exhibited a chair-like conformation, where the methyl group was away from the C—H hydrogen atom of the hydrazone moiety. These authors also noticed that the hydrazone motif displayed an *E*-configuration, which was later confirmed by Holtzer through nuclear Overhauser effect NMR experiments [18].

The original crystal form is the only known solid phase of NFX, and no other mode of this active pharmaceutical ingredient (API), including salts, co-crystals and solvates, has been reported to date. Furthermore, despite its current relevance for the pharmaceutical arsenal, knowledge of the drug remains rather scarce and, among the relevant pharmacopeias, only the International Pharmacopeia has a NFX monograph [19].

Amorphous solids lack three-dimensional long-range order in their molecular packing, representing a random ensemble of molecular orientations, conformations, and interactions. Compared with their crystalline counterparts they are in a thermodynamically higher energy state [20]. Therefore, amorphous solids exhibit an increased dissolution rate and better solubility, but also lower physical stability and usually a high propensity to crystallize [21,22].

Due to the inherent advantages of the solid state, around 80 % of all medications are enteral drug formulations (tablets, capsules, and others) [23]. The NFX drug product is available as tablets prepared from the crystal form of the API [3], and a solid formulation for pediatric use has recently been approved by the Food and Drug Administration [24]. The product has a solubility-limiting bioavailability and is prone to produce adverse effects [25,26].

The use of a more soluble form of NFX could be a suitable alternative to other approaches [27] to improve bioavailability or reduce dosage without lowering the activity of the API, and an amorphous phase may satisfy these requirements [28,29]. However, selection of this as a suitable solid phase for a dosage form requires proper characterization of the phase and detailed knowledge of its relevant properties before making the critical decision of envisaging formulation [30]. This information may also help adjust the processing conditions and anticipate or prevent unwanted solid state transformations [31].

The acquisition of detailed views of the properties of relevant amorphous solids is an important demand in the modern pharmaceutical industry [32]. Therefore, and in continuation of our previous work regarding the physicochemical properties of pharmaceutically relevant solid phases [33–35], we herein report a comprehensive analysis of the hitherto undisclosed amorphous state of NFX (AM-NFX). This study involves its preparation and characterization, as well as the evaluation of its physicochemical stability under mechanical and thermal stress conditions.

## 2. Materials and methods

### 2.1. Active pharmaceutical ingredients and chemicals

Nifurtimox bulk drug was a kind gift from Laboratorios Gador SA (Buenos Aires, Argentina). Freshly prepared double distilled water was employed for the experiments. PEG 4000 was acquired from Drogueria Saporiti (Buenos Aires, Argentina). All other solvents and reagents used were of analytical grade.

### 2.2. Preparation of AM-NFX

Nifurtimox (100 mg) was placed in a crystallizer and heated in a silicon oil bath at 180 °C, until complete melting of the solid was observed. Then, the crystallizer was removed from the bath and cooled in an ice-water bath for 10 min. The samples were triturated lightly, sieved, and stored in a desiccator. The solids were subjected to the characterization studies within the first hour after their preparation.

### 2.3. Preparation of a polymeric amorphous solid dispersion with PEG 4000

A homogeneous mixture was obtained by gentle grinding a mixture of PEG 4000 (800 mg) and NFX (200 mg) in a mortar for 3 min. The mixture was then placed in an aluminum container and heated in a dry block heater at 180 °C for 10 min until complete melting of the solid was observed. Subsequently, the molten mixture was allowed to cool down to room temperature for 20 min the resulting solid was stored in a desiccator during the experiment.

### 2.4. Sieving and mixing

The solids were sieved with an RR1920 Zonitest vibration system (Rey & Ronzoni, Buenos Aires, Argentina), fitted with ASTM-certified stainless steel sieves the 100–140 mesh fractions were used for the experiments. All samples were gently mixed in a rotatory Z mixer at 40 rpm for 30 min.

### 2.5. Hot-stage microscopy

The studies were performed with a model 350 Ernst Leitz hot-stage polarized light microscope (Ernst Leitz, GmbH, Wetzlar, Germany), heating at 2.5 °C $min^{-1}$ between 50 °C and 185 °C. The experiments were monitored with a Beion CMOS digital camera (Shanghai Beion Medical Technology Co., ltd., Shanghai, China) at a 5.0 Megapixel resolution (2592 × 1944, H × V).

### 2.6. Powder X-ray diffractometry

The powder X-ray diffractometry (PXRD) studies were performed at room temperature using a Panalytical Empyrean diffractometer (Malvern Panalytical ltd., Malvern, UK) fitted with a divergence incident slit of 0.5° and a PixCel 3D detector, operating at 40 kV and a current of 30 mA. The samples were placed in an aluminum sample holder. The data were acquired over the 2θ range of 5°–45°, at a scanning step of 0.026°, employing Cu Kα radiation (1.54184 Å) from a Ni-filtered source, with a counting time of 176 s.

### 2.7. Nuclear magnetic resonance

The $^{13}C$ (100.73 MHz) and $^{15}N$ (40.60 MHz) solid state NMR spectra were obtained with the cross-polarization at the magic angle spinning (CP-MAS) technique, on a Bruker WB 400 spectrometer (Bruker Biospin, Rheinstetten, Germany), at 27 °C using a 4-mm DVT probehead. The solid samples (~100 mg) were very gently powdered in a mortar, packed in 4-mm diameter cylindrical standard zirconium rotors ($ZrO_2$), and sealed with Kel-F caps. The $^{13}C$ spectra were referenced to a glycine sample and then the chemical shifts were recalculated to TMS, considering $\delta_{(Gly/C{=}O)}$ = 176.1 ppm. The $^{15}N$ spectra were related to $^{15}NH_4Cl$ and then converted to the $MeNO_2$ scale using the following relationship: $\delta\ ^{15}N_{(NO2Me)} = \delta\ ^{15}N_{(NH4Cl)} - 338.1$ ppm.

The typical acquisition parameters for $^{13}C$ CP-MAS were $^{1}H$ 90° pulse: 3.2 μs decoupling sequence: SPINAL 64 spectral width: 40 kHz recycle delay: 5 s acquisition time: 30 ms contact time: 2 ms and spinning rate: 12 kHz. The typical acquisition parameters for $^{15}N$ CP-MAS were $^{1}H$ 90° pulse: 3.2 μs decoupling sequence: SPINAL 64 spectral width: 40 kHz recycle delay: 5 s acquisition time: 35 ms contact time: 7 ms and spinning rate: 6 kHz.

To monitor the stability of AM-NFX, the $^{13}C$ ss NMR spectra of the sample (~100 mg) were acquired with $d_1$: 5 s at a rotation rate of 12 kHz. Spectra were recorded every 30 min between 0 and 21 h (360 scans/spectrum) and then every hour between 22 and 52 h (720 scans/spectrum).

The solution spectra (400.13 MHz for $^{1}H$, 100.73 MHz for $^{13}C$ and 40.60 MHz for $^{15}N$) were acquired at 27 °C in a 400 MHz Bruker

Avance III spectrometer (Bruker Biospin, Rheinstetten, Germany), with the samples dissolved in $CDCl_3$ ($^1H$ and $^{13}C$) or DMSO-$d_6$ ($^{15}N$). The chemical shifts are expressed in ppm (δ scale) with regards to TMS, whereas the scalar coupling constant (*J*) values are informed in Hertz.

### 2.8. Mid- and near- infrared spectroscopy

The mid-infrared (MIR) spectra were obtained in a Shimadzu Prestige 21 FTIR instrument (Shimadzu Corp., Kyoto, Japan) fitted with a controlled temperature diamond-based ATR accessory (GladiATR, Pike Technologies, Madison, USA). A fixed number of 20 scans per sample were acquired, over a wavenumber range of 3500–600 $cm^{-1}$, with a resolution of 4 $cm^{-1}$.

The near infrared (NIR) spectra were obtained at room temperature in the reflectance mode with a NIRS DS2500 (FOSS, Hillerød, Denmark) spectrometer, in the spectral range of 1000–2500 nm, at a resolution of 0.5 nm. The samples (~ 500 mg) were placed in a circular quartz cell for solids, taking an average of 7 scans/spectrum.

### 2.9. Thermal analysis

The thermogravimetric analysis (TGA) was carried out with the aid of a TA Instruments Q600 apparatus (TA Instruments, New Castle, USA). The sample (~ 8 mg) was placed in an alumina crucible and heated from room temperature to 360 °C at a rate of 5 °C $min^{-1}$ under a nitrogen atmosphere (flow rate: 100 ml $min^{-1}$).

The differential scanning calorimetry (DSC) curves were acquired with a Linseis PT1000 apparatus (Linseis Messgeraete GmbH, Selb, Germany), operating under a constant nitrogen flow (130 ml $min^{-1}$). The samples (~5 mg) were placed in open aluminum pans and heated at a rate of 5 °C $min^{-1}$ between 40 and 200 °C, using an empty open pan as the reference. The temperature axis was calibrated using an indium standard.

### 2.10. Powder dissolution rate

The determinations were performed with a Hanson SR8-Plus dissolution station (Hanson Research, Chatsworth, USA), configured as USP apparatus II (paddles). The dissolution medium (900 ml) was acetate buffer (0.05 M, pH 4.5) at 37 ± 0.5 °C and the paddle rotation rate was 100 rpm [15].

Each sieved powder sample (150 mg) was placed in an Eppendorf tube, accurately weighed with an Ohaus Explorer analytical balance (Ohaus Corp., Parsippany, NJ, USA) and then dropped onto the surface of the dissolution medium, where it became quickly and homogeneously dispersed. Aliquots of the medium (3 ml) were taken at preestablished times, filtered through 0.45 μm PTFE syringe filters, discarding the first ml, and diluted as required with dissolution medium. The NFX content was determined with an Agilent 8453 diode-array UV–vis spectrophotometer (Agilent Technologies, Santa Clara, USA), fitted with a quartz cell of 10 mm optical path length. The absorbances were measured at 403 nm against a blank of dissolution medium. The determinations were carried out in triplicate, taking the average.

### 2.11. Equilibrium solubility

Each solid sample (~100 mg) of NFX and AM-NFX was added to distilled water (10 ml) contained in a 25 ml glass vial, fitted with a Teflon-coated magnetic stirring bar. The flask was closed and immersed in a water bath and kept at 25 °C with a temperature-controlled Polyscience model 900 circulator-bath (Cole Parmer, Vernon Hills, IL, USA). The flasks contents were stirred at 200 rpm to attain equilibrium. After 3 h, the samples were transferred to centrifuge tubes, where they were centrifuged for 10 min at 3000 rpm. The supernatants were carefully separated from the undissolved solids, which were dried in a vacuum oven at room temperature and 50 mm Hg for 1 h, before being analyzed by ATR-MIR.

Aliquots of the supernatants were taken and diluted with distilled water their absorbances were acquired at 403 nm, on an Agilent 8453 diode-array UV–vis spectrophotometer (Agilent Technologies, Santa Clara, USA), against a blank of water. The amount of dissolved NFX in each case was determined by interpolation of the absorbance data of the supernatant samples in a concomitantly prepared calibration curve. The experiments were carried out in triplicate.

### 2.12. Chemometrics and graphics software

The NMR spectra were acquired and analyzed using the Topspin v.4.1.3 (Bruker) software. The chemometric analyses were carried out with the aid of MCR-ALS GUI 2.0 (available at https://mcrals.wordpress.com/download/). Spectral data management and the MCR-ALS method were run in the Matlab R2015a (Mathworks, Natick, USA) environment. Statistical data analyses and graphics were performed using Origin 8.5 (OriginLab Co., Northampton, USA).

## 3. Results and discussion

### 3.1. Characterization of AM-NFX. Comparison with commercial NFX

Solid state characterization is multidimensional and requires the combined use of various orthogonal methodologies [36]. Considering that the solid state characterization of NFX is still fragmentary and little information is available, some relevant details regarding this API, such as PXRD data, as well as NIR and ss NMR spectra are reported for the first time. These were included for comparison and discussion purposes with those of the new amorphous phase.

#### 3.1.1. Thermal analysis

Fig. 1 presents the thermoanalytical curves obtained for the solid forms of NFX employed in the present study. The DSC curve of the commercial product displayed a single endothermic event, with $T_{onset}$ = 179 °C and a peak at 182.2 °C ($\Delta h_{fus}$ = -127 J $g^{-1}$), which was coincident with its melting point (Table S1).

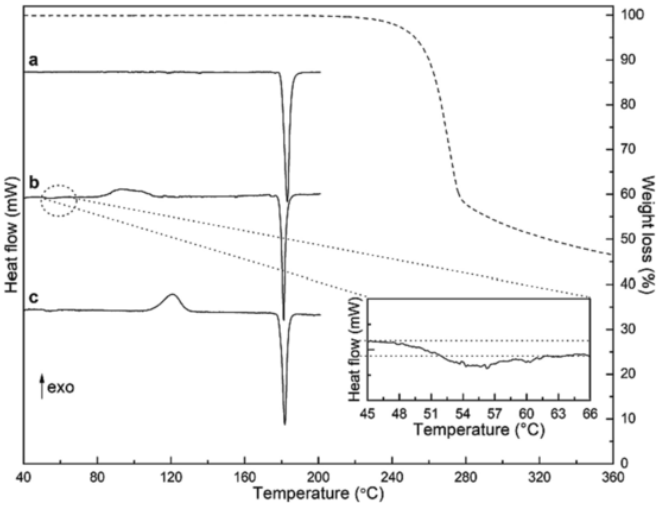


**Fig. 1.** Stacked DSC curves in the range of 40–200 °C corresponding to NFX (a), AM-NFX (b), prepared by heating a sample in an oil bath, and AM-NFX prepared *in situ*, by heating the sample in the DSC pan beyond its melting point (c). The dashed line is the TGA curve of NFX in the range 40–360 °C. Inset: Zoom of the thermal behavior of AM-NFX prepared by melting the drug in an oil bath (DSC curve b) in the region 45–66 °C ($T_g$). Dotted lines have been drawn as visual aids.

On the other hand, the curve of AM-NFX displayed three events, which included a $T_g$ at 49.9 °C ($\Delta c_p$ = 0.41 J $g^{-1}$ $°C^{-1}$), an exotherm of crystallization where the solid underwent loss of extra energy, with an onset at 84.4 °C and a peak at 93 °C ($\Delta h$ = 40 J $g^{-1}$), and an endotherm with $T_{onset}$ = 178 °C and a peak at 181.2 °C ($\Delta h_{fus}$ = -99 J $g^{-1}$), corresponding to the fusion of the solid. The behavior of this material was further confirmed with a sample of AM-NFX, which was prepared by heating the drug directly in a DSC pan, allowing the system to cool to room temperature and gently puncturing with a needle, to break the so formed solid mass.

The curve displayed the expected $T_g$ event at 50.6 °C ($\Delta c_p$ = 0.45 J $g^{-1}$ $°C^{-1}$), a clean exotherm of crystallization with $T_{onset}$ = 110.4 °C and a peak at 120.9 °C ($\Delta h$ = 54 J $g^{-1}$), followed by the melting endotherm with $T_{onset}$ = 178 °C and a peak at 181.8 °C ($\Delta h_{fus}$ = -95 J $g^{-1}$). The different positions of the exotherms of crystallization (Fig. 1b and 1c) are of no critical importance with regards to the identity of the solid it is known that such exotherms may have variable onset temperatures, which also depend on sample manipulation [37]. Furthermore, the MIR spectra of the samples originating these curves (Fig. 1b and 1c) are similar after the crystallization event, confirming the identity of the crystallized products.

A controlled DSC temperature cycling experiment (three cycles) was also carried out on NFX (Fig. S2). In the first cycle (Fig. S2A), the melting event was obvious in the heating stage, while the $T_g$ of the resulting amorphous material became evident during the cooling part of the cycle. Before initiating the second cycle (Fig. S2B), the so formed amorphous solid was gently punctured with a needle in order to induce complete solidification of the molten mass.

In this cycle, the $T_g$, crystallization and melting events were clearly detected upon heating, whereas a new $T_g$ event was again observed during the cooling cycle, as shown in an expanded view of the curve in the 30–80 °C region. The system displayed the same events during the third cycle (Fig. S2C) thus, formation of the amorphous phase upon heating was confirmed for each cycle. On the other hand, the TGA recording (Fig. 1) revealed that NFX melted without decomposition, turning the results of the three-cycle experiment into valid information. It also showed that decomposition of the drug occurred in a single stage it began at approximately 215 °C (~30 °C above the melting point) and exhibited a 5 % weight loss at 252 °C.

### 3.1.2. Hot-stage microscopy

In analogy with the DSC experiment, the material was gently punctured with a needle before being heated. Fig. 2 displays micrographs of the amorphous phase taken at different temperatures, under white and polarized light. A transparent and yellowish solid (Fig. 2A) was observed at 50 °C, where its lack of birefringence (Fig. 2B) suggested the presence of an amorphous state. Minor changes in shape and greater transparency were detected in the range of 70–82 °C (Fig. 2C), possibly due to variations in viscosity as a result of a glass transition.

At higher temperatures, the crystallization process yielded a yellow solid (Fig. 2D), which exhibited birefringence (Fig. 2E) the latter began to melt at 176 °C and afforded a yellowish melt at 178 °C (Fig. 2F). The events found in the hot-stage microscopy micrographs were in full agreement with those observed during the DSC study.

### 3.1.3. Mid-infrared spectroscopy

The MIR spectrum of the new solid phase was compared with that of the commercial drug (Fig. 3A), concluding that the most relevant changes took place in the fingerprint region (Table S2). In fact, both phases displayed similar absorption profiles over 3000 $cm^{-1}$, corresponding to the aromatic C—H stretching vibrations and small differences immediately below 3000 $cm^{-1}$, where the aliphatic C—H stretching vibrations take place [38]. On the other hand, AM-NFX exhibited some subtle signal displacements as well as broader and less defined signals in the 1600–600 $cm^{-1}$ region. These effects were attributed in general to packing differences due to a lack of long-range molecular order in the amorphous solid.

For example, the peak found at 1560 $cm^{-1}$ in NFX, attributed to the C═C and C═N stretching vibrations, was observed in AM-NFX as a broad band with lower intensity, which contained overlapped peaks with maxima at 1558, 1570, and 1589 $cm^{-1}$, whereas opposite shifts were observed among the asymmetric (1503 and 1508 $cm^{-1}$) and symmetric (1364 and 1358 $cm^{-1}$) stretching N—O vibration bands of the nitro moiety and the asymmetric (1288 and 1292 $cm^{-1}$) and symmetric (1117 and 1116 $cm^{-1}$) S—O stretching bands of the sulfone for NFX and AM-NFX, respectively.

However, examination of the asymmetric (1244 and 1240 $cm^{-1}$) and symmetric (1020 and 1010 $cm^{-1}$) C—O—C vibration bands of the furan ring and the C—N stretching frequency of the C—N bond of the nitro group (899 and 891 $cm^{-1}$) for NFX and AM-NFX, respectively revealed that they were all redshifted in the amorphous phase. Among other reasons, signal splitting and absorption shifts may be related to small changes in bond lengths as a result of packing modifications and loss of specific interactions, due to amorphization.

In other instances, such as in the region of 1470 $cm^{-1}$, it was observed that the counterpart of two closely absorbing peaks in NFX (1477 and 1458 $cm^{-1}$), became a single peak (broad or with a shoulder) in the spectrum of AM-NFX (1474 $cm^{-1}$) the same phenomenon was observed for the N—N stretching absorption of the hydrazone (1184 and 1203 vs 1192 $cm^{-1}$ for NFX and AM-NFX, respectively) and for the

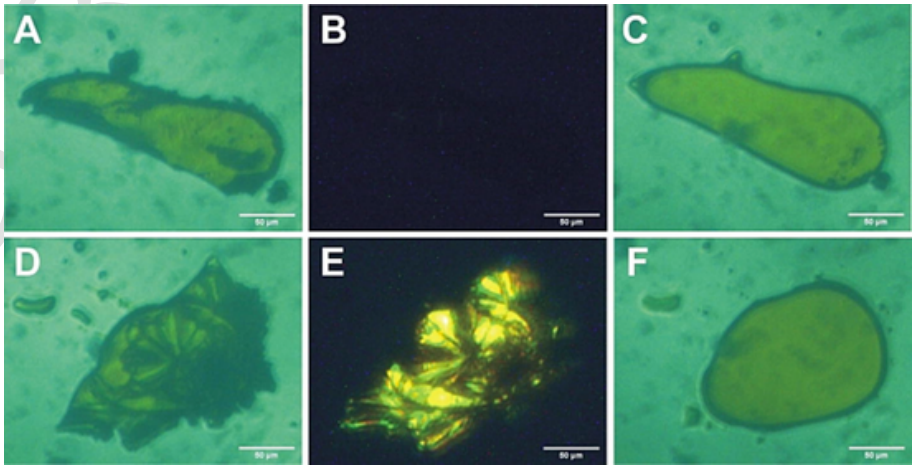


**Fig. 2.** Hot-stage microscopy micrographs of NFX at different temperatures, under white (A, C, D and F) and polarized light (B and E). A) and B) at 50 °C C) at 82 °C D) at 124 °C E) at 130 °C and F) at 178 °C.

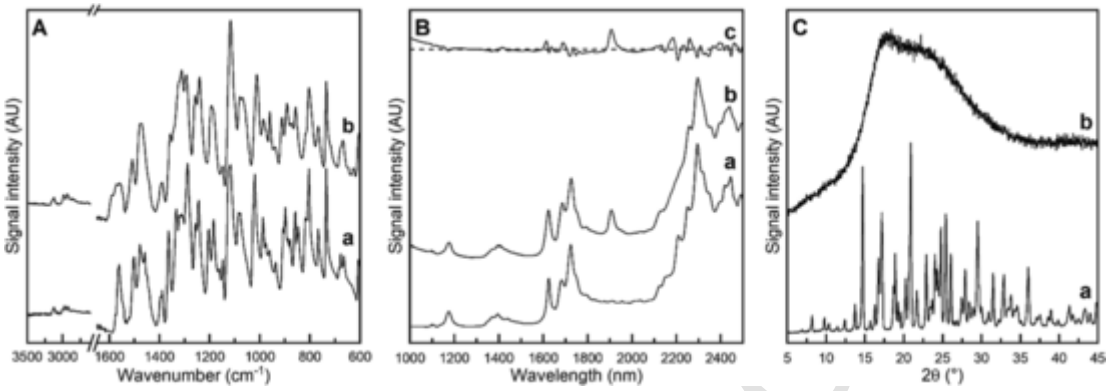


**Fig. 3.** A) Stacked MIR spectra of NFX (a) and AM-NFX (b) in the 3500–600 $cm^{-1}$ zone. B) Stacked NIR spectra of NFX (a), AM-NFX (b) and the difference between normalized spectra of AM-NFX and NFX (c) in the 1000–2500 nm range the dashed line was drawn as a visual aid. C) Stacked powder X-ray diffraction patterns of NFX (a) and AM-NFX (b) in the 2 θ = 5-45° region.

band found at 669 $cm^{-1}$ in AM-NFX, related to the symmetric C—S—C stretching vibration, which appeared as peaks at 665 and 677 $cm^{-1}$ in NFX. In addition, the prominent band found around 1332 $cm^{-1}$ in NFX was missing in the amorphous sample, probably because of overlap with neighbouring bands instead, the latter phase was characterized by a peak at 1312 $cm^{-1}$.

Furthermore, in addition to those already mentioned, there were clear differences in the 1050–750 $cm^{-1}$ zone. Despite both spectra displayed the pair of characteristic bands of 2,5-disubstituted furans at the same position (961 and 938 $cm^{-1}$) and their peak shape and intensity were alike the same observation was made regarding the couple of characteristic furan peaks found at 818 and 768 $cm^{-1}$. Taken together, these modifications can be assigned to the loss of long-range molecular order and the lack of interactions specific to the crystal form.

### 3.1.4. Near-infrared spectroscopy

NIR spectroscopy, which is sensitive to inter-and intra-molecular interactions and conformational changes, deals with the overtones and combination bands of the stretching and bending non-harmonic vibrations observed in the MIR region [39]. Few hydrazone derivatives have been studied by NIR spectroscopy [40,41], and to the best of our knowledge, none of them in the full spectral range (700–2500 nm). Therefore, the literature contains very scarce information about their characteristic absorptions.

The NIR spectra of NFX and AM-NFX, shown in Fig. 3B, displayed broad and overlapped peaks, a common feature of this spectroscopy not unexpectedly, both spectra were very similar and exhibited only subtle differences, which may be useful for identification and quantification of these solid state phases.

Both spectra exhibited absorptions (Table S3) which can be attributed to CH-CH and CH-CC combination bands (2200–2500 nm), as well as to the first (1600–1800 nm) and second (1150–1450 nm) overtones of the C—H stretching vibration in the $CH_3$, $CH_2$, and CH motifs. In addition, peaks found at 1625/1624 nm and 1106/1103 nm were related to the first and second overtones of the aromatic C—H stretching vibration (ArH) of the hydrogens associated with the furan ring. Subtraction of normalized spectra of both phases highlighted the most obvious NIR spectral differences, including changes in absorption wavelength and intensity.

In addition to these major spectral differences, some peaks present in NFX (for example those at 1439, 2150, 2210 and 2320 nm) and missing in AM-NFX were detected, along with changes in peak positions the peaks at 2417, 2445 and 2491 nm in NFX have their counterparts at 2420, 2439 and 2496 nm, respectively, in AM-NFX).

Despite both spectra displayed an upward shift in their baselines, with an increasing magnitude toward longer wavelengths, it was easy to observe a distinct upward baseline shift in the spectrum of AM-NFX in the lower wavelength region (1000–1100 nm). In addition, AM-NFX displayed a prominent peak at 1908 nm which was not seen in the crystalline material and proved to be a good marker for the presence of the amorphous state. This combination band is probably related to the C═N moiety of the hydrazone [42]. These features reflect the impact of crystallinity (or its absence) on the vibrational properties of the corresponding solids.

### 3.1.5. Powder X-ray diffraction

Fig. 3C displays the diffraction patterns obtained by PXRD for commercial NFX and for the amorphous solid resulting from the heat treatment. The commercial form of the drug proved to be a crystalline phase, which presented a rich pattern, with sharp and narrow peaks at characteristic Bragg diffraction angles (2θ). The peaks, which were of different intensity, were classified as small: 8.2, 9.8, 10.4, 11.5, 12.4, 13.7, 15.7, 16.3, 18.7, 19.3, 19.6, 20.3 and 21.7° medium: 16.8, 18.9, 22.9, 24.0, 26.1, 27.9, 31.5, 32.9 and 36° and large: 14.7, 17.2, 20.9, 24.8, 25.4, and 29.5°.

The experimental PXRD pattern was found to be in good agreement with that calculated from the single crystal analysis of the CCDC deposition number 1,182,040 [17]. Furthermore, the correlations with the theoretical PXRD of the drug based on the latter indicated that the most intense characteristic peaks at 2θ = 14.7 and 20.9° corresponded to the planes (1,0,1) and (1,3,0), respectively. Bragg peaks are characteristic of the long-range molecular order found in crystals, where X-rays can be constructively diffracted however, they were not observed in the diffractogram of AM-NFX, due to lack of this constructive interference, confirming its amorphous nature [43].

### 3.1.6. Solid state NMR spectroscopy

*3.1.6.1. $^{13}C$ ss NMR.* The CP-MAS $^{13}C$ spectra of NFX and AM-NFX are shown in Fig. 4A, along with a NQS (Non-Quaternary Suppression) sub-spectrum of the crystalline form. The number of signals observed in the spectrum of NFX was higher than the number of carbon atoms in the molecule. In addition, there was clear evidence of signal duplication, especially among the furan and methyl carbon atoms this is consistent with the presence of two molecules of NFX in the the asymmetric unit cell [17].

Signal separation was enough to enable their assignment with the aid of the solution spectrum and the NQS sub-spectrum. Under assistance of the latter, the two most deshielded pairs of resonances were attributed to both carbon atoms of the furan ring not attached to hydrogens (*C*2 and C5). Further support for this interpretation came from a comparison with solution spectra in $CDCl_3$ and DMSO-$d_6$ (Figs. S3 and S6), additional experiments (Figs. S4, S5 and S7-S9), and literature data of related compounds [44], which enabled unambiguous assignment of these signals (Table S4). On the other hand, and in agreement with the

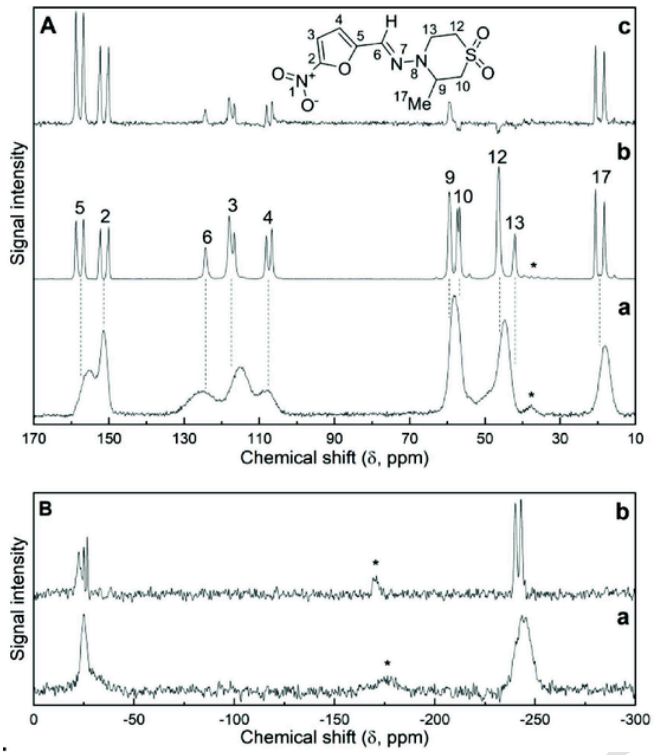


**Fig. 4.** A) Stacked $^{13}$C ss NMR spectra (CP-MAS technique) of: AM-NFX (a), NFX (b), and NFX (NQS experiment) for identification of quaternary (C5, *C2*) and methyl (C17) carbon atoms (c). B) Stacked $^{15}$N ss NMR spectra (CP-MAS technique) of AM-NFX (a) and NFX (b). Asterisks denote spinning sidebands. Dashed lines are drawn as visual aids. Atoms were numbered according to Elguero *et al.* [17].

solution spectrum, the remaining more shielded aromatic signals were assigned to the other pair of carbon atoms of the furan ring (C3 and C4), whereas the resonance at $\delta$ = 124.9 ppm was attributed to the hydrazone carbon atom (C6).

It has been pointed out that efforts on ss NMR resonance attribution of amorphous active pharmaceutical ingredients are rarely seen, because of the challenge represented by peak assignment from broad linewidths such peaks arise from a large distribution of chemical environments distributed at random, an effect that is not averaged out by the magic angle spinning setup [45,46]. However, the spectrum of AM-NFX seemed to be simple enough to attempt assignment.

Compared with the $^{13}$C ss NMR spectrum of NFX, the spectrum of AM-NFX displayed fewer resonances than those expected, which were observed as broad peaks, in agreement with the non-crystalline nature of the sample. The resonances of C9 and C10 appeared as a single signal at $\delta$ = 58.3 ppm, and the same occurred with the peaks corresponding to the methyl group ($\delta$ = 18.5 ppm), whereas those belonging to the furan ring were observed as two pairs of overlapped signals, with those of the CH carbon atoms being more shielded than their counterparts substituted by the nitro and hydrazone moieties.

*3.1.6.2. $^{15}$N ss NMR.* Relatively few hydrazones have been studied by $^{15}$N NMR spectroscopy, and even fewer have been examined at the solid state [47,48]. Fig. 4B displays the $^{15}$N ss NMR spectra of crystalline and amorphous NFX (CP-MAS technique). In the case of the crystalline material, well-defined peaks corresponding to the three nitrogen atoms were observed, which were assigned with the help of the solution $^{15}$N HMBC spectrum of NFX (Figs. S10 and S11). Table 1 contains the complete $^{13}$C and $^{15}$N assignments of crystalline and amorphous NFX and a comparison with data of the corresponding solution spectra.

**Table 1**
Assignment of $^{13}$C and $^{15}$N ss NMR signals of crystalline and amorphous nifurtimox. Comparison with the solution spectra.[a]

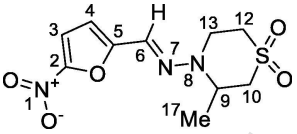

| Position N° | Solution ($CDCl_3$) | Solid phase | | Position N° | Solution ($CDCl_3$) | Solid phase | |
|---|---|---|---|---|---|---|---|
| | | NFX | AM-NFX | | | NFX | AM-NFX |
| 1 | -[b] | −22.4 | −25.9 | 8 | −246.6[b] | −240.1–243.0 | −244.4–246.0 |
| 2 | 151.4 | 152.2 150.1 | 151.4 | 9 | 57.8 | 59.5 | 58.3 |
| 3 | 113.9 | 118.0 116.7 | 114.5 | 10 | 56.5 | 57.3 56.8 | 58.3 |
| 4 | 108.9 | 108.1 106.7 | 107.6 | 12 | 45.4 | 46.3 | 44.8 |
| 5 | 154.0 | 158.7 156.8 | 155.4 | 13 | 43.6 | 42.0 | 44.8 |
| 6 | 125.0 | 124.3 | 124.9 | 17 | 17.7 | 20.6 18.3 | 18.5 |
| 7 | −29.2[b] | −25.0–26.7 | −25.9 | | | | |

[a] Chemical shifts are in the δ scale, in ppm.
[b] From a $^{15}$N HMBC experiment in DMSO-$d_6$. The signal of the $^{15}NO_2$ (N1) could not be detected.

The single and rather broad signal at δ = –22.4 ppm was assigned to the nitrogen atom of the nitro group (N1) whereas the couple of well differentiated duplicate peaks were attributed to the hydrazone nitrogen atoms (N7 and N8). The most shielded pair of signals (δ = -240.1 and −243.0 ppm) was assigned to N8 while the most deshielded pair of peaks (δ = -25.0 and −26.7 ppm) was attributed to the $N_{sp}^2$ atom (N7) [49], whose resonance neared that of N1, in agreement with literature precedents [50].

As expected, the peaks of AM-NFX were broader, to the point that the $^{15}$N signals of the nitro moiety and the $N_{sp}^2$ hydrazone (N7) atom became a single resonance at δ = -25.9 ppm. Interestingly, N8 appeared as two strongly overlapped broad signals peaking at δ = -244.4 and −246.0 ppm. The subtle shielding of N8 in this phase with regards to the crystalline material along with the resonance shifts of N1 and N7 and the $^{13}$C ss NMR observations, collectively evidenced that amorphization involves the loss of specific interactions as a result of differences in molecular packing, which yields broader signals [51].

*3.1.6.3. Powder dissolution rate and solubility.* The determination of the powder dissolution rate is a convenient alternative for evaluating the oral bioavailability of drugs [52,53]. The strategy has been used for poorly soluble products [54]. Considering that compression may impact the stability of AM-NFX, gently sieved powders of the latter along with crystalline NFX were subjected to dissolution tests under sink conditions, and the results are shown in Fig. 5.

Linear fits of the initial datapoints, obtained within the first hour, revealed that the dissolution rates of the crystalline and amorphous powders were 3.81 X $10^{-3}$ mg $s^{-1}$ and 8.34 X $10^{-3}$ mg $s^{-1}$, respectively. Not unexpectedly, this meant that the dissolution rate of AM-NFX was ~ 2.2 times greater than that of the crystal form. Other API, like sodium furosemide salt exhibited similar rate improvement [55], as part of a general phenomenon [56]. The same trend was observed at the 150 min timepoint, when the amounts of drug dissolved were 19.3 % and 31.5 % for the crystalline and amorphous powders, respectively (~63 % increased rate).

On the other hand, the equilibrium solubility of both solid forms was assessed using the shake flask method [57], in order to evaluate potential solubility advantages of AM-NFX. The solubility of NFX was found to be 34.0 ± 0.2 μg $ml^{-1}$, whereas that of AM-NFX was deter-

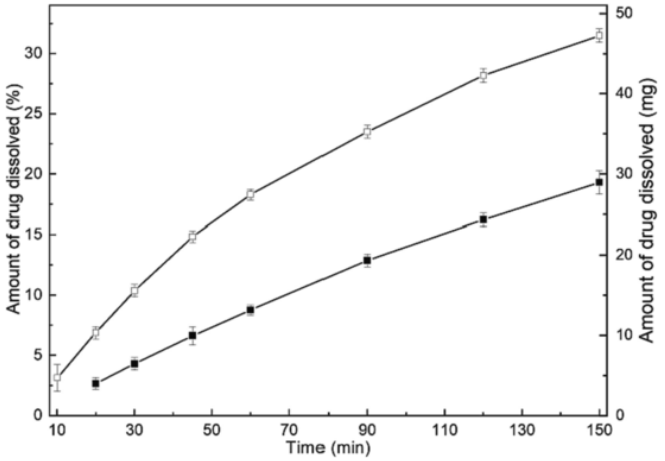


**Fig. 5.** Powder dissolution rates of NFX (■) and AM-NFX (□).

mined as 46.4 ± 0.3 μg ml$^{-1}$. In addition, in the latter case, the undissolved solid was visually inspected and analyzed by ATR-MIR (Fig. S12) furthermore, linear regression analyses were performed between the spectrum of the undissolved solid and the pure spectra of AM-NFX and NFX acquired under analogous conditions.

Considering the 1600–600 cm$^{-1}$ region (519 datapoints/spectrum), the statistical comparison against AM-NFX afforded $r^2$ = 0.9945, whereas against NFX it was found $r^2$ = 0.8213, concluding that no significant phase transformation took place during the experiment (Figs. S13 and S14). Therefore, in the absence of a solution-mediated phase transformation during the analysis of the amorphous phase, the obtained value can be considered an accurate representation of the solubility of AM-NFX.

Under sink conditions, the dissolution rate of a solid (DR) is proportional to the thickness of the diffusion layer (h) as well as to the diffusivity of the solid (D) and its solubility (s) therefore, DR = K*D*h*s. It has been proposed that when the hydrodynamic conditions of the dissolution experiment are controlled to be analogous, the mass flux ratio between two dissolving solids (1 and 2) relates to their solubility ratio thus $DR_1/DR_2 = s_1/s_2$ [58,59]. In addition, under these conditions, the maximum concentrations of dissolved solids measured in the dissolution rate experiments should represent their corresponding equilibrium solubilities [60].

Interestingly, Weibull fits of the powder dissolution curves (Fig. S15) confirmed this proposal, predicting solubility values of 47.0 and 35.1 μg ml$^{-1}$ for AM-NFX and NFX, respectively. Furthermore, their corresponding ratio ($DR_1/DR_2$ = 1.34) was in good agreement with the experimentally determined equilibrium solubility ratio ($s_1/s_2$ = 1.36).

### 3.2. Stability of the amorphous phase

#### 3.2.1. Thermal and mechanical stress

In the modern pharmaceutical industry, there is always a need to know about the stability of amorphous drug candidates early in the formulation process [31]. Hence, the stability of AM-NFX was monitored through the use of thermal and spectroscopic means. The series of DSC scans shown in Fig. 6A revealed that the intensity of the crystallization exotherm, characteristic of AM-NFX, fades with time, as it underwent a slow transformation into the crystalline material. It was still visible after one month, but undetectable in the two-month scan.

The ss NMR monitoring of AM-NFX unveiled a similar event. Periodic acquisition of $^{13}$C CP-MAS spectra at ambient temperature revealed that AM-NFX suffered phase conversion at a higher rate than that in the DSC case (Fig. 6B). Most probably, the mechanical stress during sample preparation and the higher internal temperatures (~50 °C) caused by rotor movement at 12 kHz could be at the root of this devitrification rate acceleration.

Grinding is a known pharmaceutical process, used to accelerate the dissolution of materials by reducing their particle size. This operation may cause or enhance amorphization [61,62], and can also promote form conversion [63], including devitrification [64,65]. Reduction of AM-NFX to a fine powder in an agate mortar for 15 min fully confirmed that the phase is sensitive to pressure and mechanical stress. This treatment clearly accelerated phase conversion and the material resulted in a solid, which gave a $^{13}$C ss NMR spectrum very similar to that of the commercial crystalline product (Fig. 6C).

On the other hand, the NIR spectra, which require less manipulation for sample preparation, revealed the same phase transformation, albeit at a significantly slower pace, taking over 4 weeks to reach completion (Fig. 7A). Further evidence of this phenomenon was collected when the amorphous phase was monitored by ATR-MIR spectroscopy (Fig. 7B).

Initial application of pressure induced such stress that it triggered the deamorphization process. After 29 h, the reversion was almost complete, as judged from the presence of most of the subtle features of the crystalline phase in the spectrum. It should be noted that the NIR and MIR experiments to monitor the effects of mechanical stress (Fig. 7A and 7B) were conducted below $T_g$.

#### 3.2.2. Stability of the polymeric amorphous solid dispersion AM-NFX/PEG 4000

In order to further test the stability of the amorphous phase, a series of experiments with mixtures of PEG and AM-NFX in different proportions were performed (Fig. S16) to ensure the presence of the latter. As

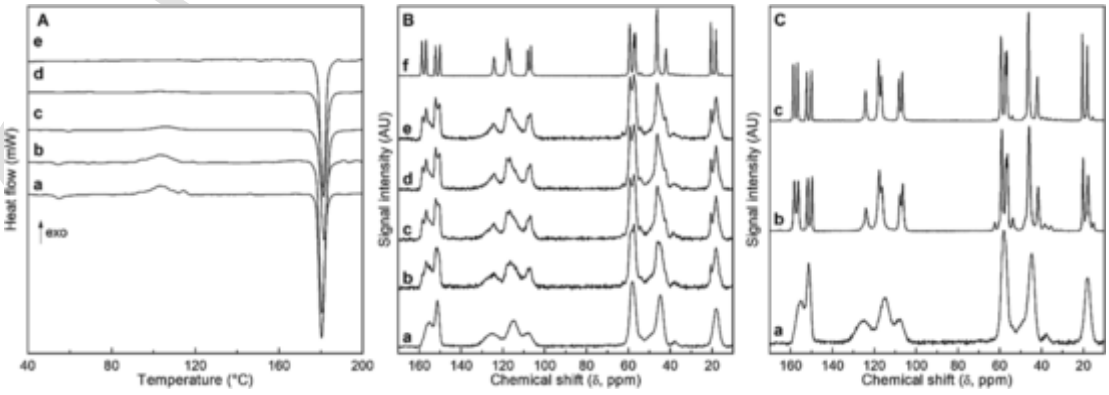


**Fig. 6.** Monitoring of the stability of AM-NFX under different conditions. A) Stacked DSC curves at 3 d (a), 8 d (b), 16 d (c), 30 d (d) and 60 d (e). B) Stacked $^{13}$C ss NMR at 2 h (a), 12 h (b), 22 h (c), 42 h (d), and 52 h (e), compared with crystalline NFX (f). C) Stacked $^{13}$C ss NMR of freshly prepared AM-NFX (a), the amorphous phase after being grinded for 15 min in an agate mortar (b), and NFX, crystalline phase (c).

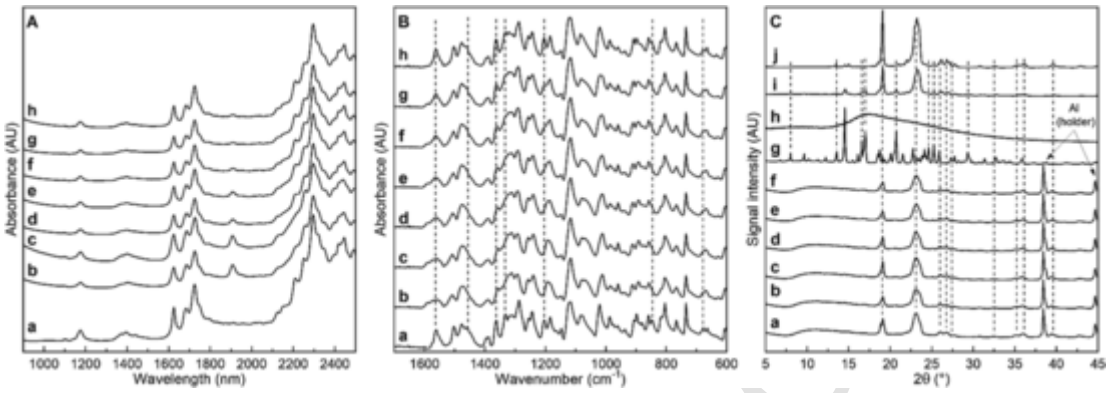


**Fig. 7.** A) Time-dependent evolution of the NIR spectra of amorphous NFX. Comparison of the crystalline form (a) with AM-NFX after 1 d (b), 2 d (c), 3 d (d), 1 week (e), 2 weeks (f), 3 weeks (g) and 4 weeks (h). B) Time-dependent evolution of the ATR-MIR spectra of amorphous NFX. Comparison of the crystalline form (a) with AM-NFX after 1 h (b), 3 h (c), 5 h (d), 6 h (e), 7 h (f), 8 h (g) and 29 h (h). C) PXRD analysis of the stability of the 1:4 (*w/w*) polymeric amorphous solid dispersion of AM-NFX in PEG 4000 after 5 days (a), 12 days (b), 19 days (c), 26 days (d), 33 days (e) and 40 days (f) comparison with the diffractograms of NFX (g), AM-NFX (h), physical mixture (4:1 *w/w*) of PEG 4000 and AM-NFX (i), and PEG 4000 (j). Dashed lines were drawn as visual aids.

a result, a (1:4, *w/w*) polymeric amorphous solid dispersion [66] of AM-NFX in PEG 4000 (slight excess of the dispersing agent) was prepared as a proof of concept and examined by PXRD. The work of Hempel *et al.* was followed [67], and gentle grinding of the solids in an agate mortar followed by melting of the mixture was employed as preparation method.

As shown in Fig. 7C, after periodically collecting PXRD data at room temperature, it was observed that the diffractograms remained consistent for 40 days, not showing evidence of a crystalline NFX phase. Furthermore, when a diffractogram of the sample acquired with improved resolution in the range 2 θ = 7-14° was examined (Fig. S17B), no signs of a crystalline NFX phase were detected. Only signals of PEG 4000 could be detected during these experiments, as a result of the proportion in which the excipient was present (Fig. 7C and S17B).

This evidence suggested that phase stabilization of AM-NFX can be achieved when it is formulated alongside a suitable co-former. Additionally, sujection of the polymeric amorphous solid dispersion AM-NFX/PEG 4000 to the dissolution conditions previously used for NFX and AM-NFX, resulted in essentially complete dissolution in approximately 10 min (Fig. S18).

### *3.2.3. Chemometrics-assisted spectroscopic monitoring of the thermal stability*

The DSC (Fig. 1) and $^{13}$C ss NMR (Fig. 6B) experiments suggested that application of heat can accelerate conversion of AM-NFX into NFX and similar phase reversions have been tracked by PXRD and MIR spectroscopy [68]. Considering that the comparison between spectra of both phases (Fig. 3A) revealed that they contain differential features, a variable temperature ATR-MIR approach to monitor the reversion of AM-NFX to the crystalline phase was put in place.

Accordingly, a series of 45 spectra were acquired every 3 °C in the 30–162 °C interval (Fig. S19) due to their high similarity and important signal overlapping, in order to unveil the sought information about the abundance of the species they were subjected to a chemometric processing using the MCR-ALS algorithm, with the results shown in Fig. 8.

Before running the algorithm, the spectra were arranged matrix-wise and pre-treated. They were edited, leaving only their informative fingerprint regions (1600–600 cm$^{-1}$), and subjected to multiplicative scatter correction. In addition, non-negativity, unimodality, and closure in the concentration profiles along with spectral non-negativity were applied as restrictions to the algorithm to ensure the physicochemical sense of the results [34,35].

The number of components was established as three based on the single value decomposition of the input matrix (explained variance: 99.1 %), and in agreement with the interpretation of the DSC curves. In addition, the Simplisma purity function was employed for variable selection in order to initialize the MCR algorithm [69].

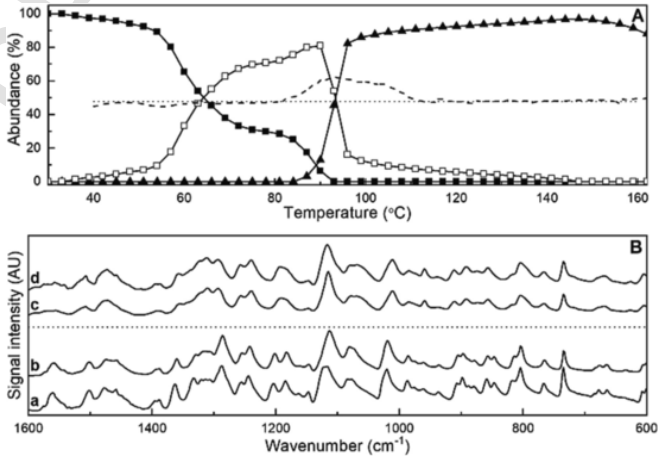


**Fig. 8.** A) MCR-ALS analysis of ATR-MIR spectra for the monitoring of the temperature-mediated reversion of AM-NFX (■) to the crystalline state (▲) through the intermediacy of a second amorphous absorbing species (□). The DSC curve ( – – –) of AM-NFX was superimposed to aid interpretation. B) Pairwise comparison between the MIR spectra of the components calculated by MCR-ALS: NFX (a) vs NFX/MCR-ALS (b) and AM-NFX (c) vs AM-NFX/MCR-ALS (d). Dotted lines were drawn as visual aids.

The estimations of the abundance profiles of the different species were provided by MCR-ALS (Fig. 8A), where the observed value of the lack of fit (LOF: 2.99 %) indicated that the MCR-ALS fit to the experimental data matrix was of high quality. In agreement with the DSC curve of AM-NFX, the graphs revealed that the initial amorphous species becomes engaged in a conversion process at ~ 50 °C, which involves the $T_g$ event.

Based on the spectroscopic characteristics of the sample, MCR-ALS was capable of detecting the presence of a new absorbing species, in coincidence with the observations made by hot-stage microscopy [35]. Formation of the latter amorphous was concomitant with depletion of the initial AM-NFX until ~ 90 °C, when conversion into the crystalline phase acquired importance, in agreement with the presence of the crystallization exotherm in the DSC curve.

On the other hand, the MCR-calculated spectra of the initial and final species involved in phase conversion are displayed in Fig. 8B. Visual and pairwise statistical comparisons [70] confirmed the identity of the

latter as NFX ($r = 0.983$, $n = 526$) and AM-NFX ($r = 0.914$, $n = 526$), respectively.

## 4. Conclusions

Nifurtimox, a poorly soluble nitrofuran hydrazone derivative, is one of the only two drugs available for treatment of specific stages of Chagas disease. Aiming to find a more soluble alternative of the drug, the amorphous phase of nifurtimox was prepared and characterized by comparison with the crystalline material, employing microscopic, spectroscopic, thermal and diffractometric means.

The near- and mid- infrared spectroscopies revealed signal broadening and the presence of subtle characteristic absorption differences, reflecting the increase of disorder associated to the phase transition process and changes in molecular interactions, whereas the wide bands found in the solid state $^{13}C$ NMR spectrum and the halo observed in the powder X-ray diffractogram highlighted the lack of long-range order in the amorphous solid. In addition, the amorphous material proved to be more soluble than the commercial substance, whereas the powder dissolution test revealed that the initial dissolution rate of AM-NFX is more than twice that of the crystalline material.

The stability of the amorphous phase was also examined, observing that the solid was highly unstable, being able to spontaneously revert to the original crystalline state at room temperature, and that this devitrification was accelerated under mechanical and thermal stress conditions. The thermally-induced phase reversion process was studied by a chemometrics-assisted analysis of MIR spectra taken at different temperatures, which also confirmed the events observed in the DSC curve of AM-NFX. On the other hand, as a conceptual proof, it was demonstrated that AM-NFX can be stabilized through formation of a polymeric amorphous solid dispersion with PEG 4000.

These preliminary results indicate that the amorphous form of nifurtimox may be a suitable alternative to alleviate solubility issues of this drug, and suggest that its use could be made possible by stabilization of this phase through a proper formulation design.

## CRediT authorship contribution statement

**Aldana B. Moroni :** Methodology, Formal analysis, Investigation, Data curation, Writing – original draft, Writing – review & editing, Visualization. **Elena Perez Mayoral :** Conceptualization, Formal analysis, Resources, Writing – original draft, Writing – review & editing, Supervision. **Diego F. Lionello :** Methodology, Formal analysis, Investigation, Data curation, Writing – review & editing, Visualization. **Daniel R. Vega :** Conceptualization, Formal analysis, Resources, Writing – original draft, Writing – review & editing, Supervision. **Teodoro S. Kaufman :** Conceptualization, Formal analysis, Resources, Writing – original draft, Writing – review & editing, Visualization, Supervision, Project administration, Funding acquisition. **Natalia.L. Calvo :** Conceptualization, Methodology, Formal analysis, Investigation, Resources, Data curation, Writing – original draft, Writing – review & editing, Visualization, Supervision, Project administration, Funding acquisition.

## Declaration of Competing Interest

The authors declare that they have no known competing financial interests or personal relationships that could have appeared to influence the work reported in this paper.

## Data availability

Data will be made available on request.

## Acknowledgements

The authors gratefully acknowledge Consejo Nacional de Investigaciones Científicas y Técnicas (CONICET, PUE IQUIR 2016), Agencia Nacional de Promoción Científica y Tecnológica (ANPCyT, PICT 2019-1155), Agencia Santafesina de Ciencia, Tecnología e Innovación (ASaCTeI, IO-2019-302) for financial support. NLC thanks to Carolina Foundation and the Argentine Ministry of Education for the Mobility Program for Argentine Teachers. ABM is also thankful to CONICET for her Doctoral fellowship. The capable assistance of Dr. M. A. García Fernández (NMR Service, UNEDLAB, UNED) and Cristian Oubiña (XRD Service, CAC, CNEA), and the kind provision of nifurtumox (Drs. D. Tombari and M. B. García, Laboratorio Gador SA, Argentina) are also gratefully acknowledged.

## Appendix A. Supplementary data

Supplementary data to this article can be found online at https://doi.org/10.1016/j.ejpb.2023.01.008.

## References

[1] H. Herlinger, K.-H. Mayer, S. Petersen, M. Bock, Verfahren zur Herstellung von 5-Nitro-furfuryliden-(2)-iminoderivaten. Patent DE 1170957, 1964 to Bayer A.G.
[2] H. Herlinger, K.-H. Mayer, S. Petersen, M. Bock, Novel 5-nitro-furfurylidene-(2)-derivatives and process for producing the same. Patent US 3262930, 1966 to Bayer A.G.
[3] World Health Organization. (2021). World Health Organization model list of essential medicines: 22nd list (2021). World Health Organization. Available at: https://apps.who.int/iris/handle/10665/345533 (accessed 23.12.22).
[4] C.J. Schofield, J. Jannin, R. Salvatella, The future of Chagas disease control, Trends Parasitol. 22 (2006) 583–588, https://doi.org/10.1016/j.pt.2006.09.011.
[5] R. Thakare, A. Dasgupta, S. Chopra, Update on nifurtimox for treatment of Chagas disease, Drugs Today 57 (2021) 251–263, https://doi.org/10.1358/dot.2021.57.4.3251712.
[6] WHO. Chagas Disease (American Trypanosomiasis); WHO: Geneva, Switzerland, 2017. http://www.who.int/neglected_diseases/diseases/en/ (accessed 28.9.22).
[7] J.R. Coura, P.A. Viñas, Chagas disease: a new worldwide challenge, Nature 465 (2010) S6–S7, https://doi.org/10.1038/nature09221.
[8] G.L. Saulnier Sholler, N. Swamy, S. Kalkunte, R.K. Singh, L. Brard, K.K. Kim, Nitrofuran compounds for the treatment of cancer and angiogenesis. Patent US 9220714, 2015.
[9] C. Bailly, Toward a repositioning of the antibacterial drug nifuroxazide for cancer treatment, Drug Discov. Today 24 (2019) 1930–1936, https://doi.org/10.1016/j.drudis.2019.06.017.
[10] N.A. Kasim, M. Whitehouse, C. Ramachandran, M. Bermejo, H. Lennerna, A. Hussain, H.E. Junginger, S.A. Stavchansky, K.K. Midha, V.P. Shah, G.L. Amidon, Molecular properties of WHO essential drugs and provisional biopharmaceutical classification, Mol. Pharm. 1 (2003) 85–96, https://doi.org/10.3390/scipharm85010001.
[11] C.B. Moraes, K.L. White, S. Braillard, C. Perez, J. Goo, L. Gaspar, D.M. Shackleford, A. Cordeiro-da-Silva, R.C.A. Thompson, L. Freitas-Jr, S.A. Charman, E. Chatelain, Enantiomers of nifurtimox do not exhibit stereoselective anti-Trypanosoma cruzi activity, toxicity, or pharmacokinetic properties, Antimicrob. Agents Chemother. 59 (2015) 3645–3647, https://doi.org/10.1128/AAC.05139-14.
[12] H. Kramer, K. Bauer, K. Schlossmann, W. Vater, Process for the production of solid preparations of sparingly soluble medicinally active compounds in a very finely divided form. Patent GB 1456618A, 1975.
[13] The International Pharmacopeia 10th Ed., Nifurtimox (Nifurtimoxum) monograph, WHO: Geneva, Switzerland, 2020. https://digicollections.net/phint/2020/index.html#d/ b.6.1.252 (accessed 29.09.22).
[14] A.G. Bayer, Leverkusen, Stable tablet formulation of nifurtimox and process for producing the same, Patent EP 3750527A1 (2020).
[15] H. Stass, S. Just, B. Weimann, I. Ince, S. Willmann, E. Feleder, C. Freitas, G. Yerino, U. Münster, Clinical investigation of the biopharmaceutical characteristics of nifurtimox tablets – implications for quality control and application, Eur. J. Pharm. Sci. 166 (2021) 105940, https://doi.org/10.1016/j.ejps.2021.105940.
[16] J.M. Moral Sanchez, I. Gonzalez-Alvarez, A. Cerda-Revert, M. Gonzalez-Alvarez, A. Navarro-Ruiz, G.L. Amidon, M. Bermejo, Biopharmaceutical optimization in neglected diseases for paediatric patients by applying the provisional paediatric biopharmaceutical classification system, Br. J. Clin. Pharmacol. 84 (2018) 2231–2241, https://doi.org/10.1111/bcp.13650.
[17] M.C. Foces-Foces, F. Hernandez Cano, R.M. Claramunt, A. Fruchier, J. Elguero, Molecular structure in the solid state (X-ray diffraction) and in solution ($^{1}H$ and $^{13}C$ NMR) of nifurtimox and two pyrazol-1-yl analogs, Bull. Soc. Chim. Belg. 97 (1988) 1055–1065, https://doi.org/10.1002/bscb.19810901015.
[18] W. Holzer, Determination of the stereochemistry of chemotherapeutics derived from 5-nitrofurfural: NOE difference spectroscopy as a simple and reliable method,

Arch. Pharm. (Weinheim) 25 (1992) 769–772.
[19] L. Roth, M. Adler, T. Jain, D. Bempong, Monographs for medicines on WHO's Model List of Essential Medicines, Bull. World. Health. Org. 96 (2018) 378–385, https://doi.org/10.2471/BLT.17.205807.
[20] Q. Shi, S.M. Moinuddin, Y. Wang, F. Ahsan, F. Li, Physical stability and dissolution behaviors of amorphous pharmaceutical solids: Role of surface and interface effects, Int. J. Pharm. 25 (2022) 122098, https://doi.org/10.1016/J.IJPHARM.2022.122098.
[21] L. Yu, Amorphous pharmaceutical solids: Preparation, characterization and stabilization, Adv. Drug Deliv. Rev. 48 (2001) 27–42, https://doi.org/10.1016/S0169-409X(01)00098-9.
[22] H. Grohganz, P.A. Priemel, K. Löbmann, L.H. Nielsen, R. Laitinen, A. Mullertz, G. Van Den Mooter, T. Rades, Refining stability and dissolution rate of amorphous drug formulations, Expert Opin. Drug. Deliv. 11 (2014) 977–989, https://doi.org/10.1517/17425247.2014.911728.
[23] B.M. Couillaud, P. Espeau, N. Mignet, Y. Corvis, State of the art of pharmaceutical solid forms: from crystal property issues to nanocrystals formulation, ChemMedChem 14 (2019) 8–23, https://doi.org/10.1002/cmdc.201800612.
[24] https://www.drugs.com/newdrugs/fda-approves-lampit-nifurtimox-chagas-children-5317. html. (accessed 29.08.22).
[25] C. Crespillo-Andújar, S. Chamorro-Tojeiro, F. Norman, B. Monge-Maillo, R. Lopez-Velez, J.A. Perez-Molina, Toxicity of nifurtimox as second-line treatment after benznidazole intolerance in patients with chronic Chagas disease: when available options fail, Clin. Microbiol. Infect. 24 (1344) (2018) e1–1344.e4, https://doi.org/10.1016/j.cmi.2018.06.006.
[26] Y. Li, T.-T. Liu, H.-T. Jin, P.-P. Zhang, D. Qin, Q.-Q. Zhang, W.-T. Wu, C.-P. Yang, A.-P. Wang, A comparison of toxicity and toxicokinetics in rats and dogs following twenty-eight-day, repeat-dose oral administration of nifurtimox, Toxicol. Res. 6 (2017) 544–553, https://doi.org/10.1039/c7tx00061h.
[27] G. Gonzalez-Martin, I. Merino, M.N. Rodriguez-Cabezas, M. Torres, R. Nuñez, A. Osuna, Characterization and trypanocidal activity of nifurtimox-containing and empty nanoparticles of polyethylcyanoacrylates, J. Pharm. Pharmacol. 50 (1998) 29–35, https://doi.org/10.1111/j.2042-7158.1998.tb03301.x.
[28] N.J. Babu, A. Nangia, Solubility advantage of amorphous drugs and pharmaceutical cocrystals, Cryst. Growth Des. 11 (2011) 2662–2679, https://doi.org/10.1021/cg200492w.
[29] S. Khodadadi, G.M.H. Meesters, Amorphous APIs: improved release, preparation, characterization, in: H. Merkus, G. Meesters, W. Oostra (Eds.), Particles and Nanoparticles in Pharmaceutical Products. AAPS Advances in the Pharmaceutical Sciences Series, vol. 29, Springer, Cham, Switzerland, 2018, pp. 329–346.
[30] G. Davies, Changing the salt, changing the drug, Pharm. J. 266 (2009) 322–323.
[31] M. Palucki, J.D. Higgins, E. Kwong, A.C. Templeton, Strategies at the interface of drug discovery and development: Early optimization of the solid state phase and preclinical toxicology formulation for potential drug candidates, J. Med. Chem. 53 (2010) 5897–5905, https://doi.org/10.1021/JM1002638.
[32] Amorphous Drugs: Benefits and Challenges. M. Rams-Baron, R. Jachowicz, E. Boldyreva, D. Zhou, W. Jamroz, M. Paluch (Eds.), Springer, New York, USA, 2018.
[33] D.M. Salazar-Rojas, T.S. Kaufman, R.M. Maggio, A comprehensive approach toward concomitant triclabendazole polymorphism in pharmaceutical products, J. Drug Deliv. Sci. Technol. 62 (2021) 102386, https://doi.org/10.1016/j.jddst.2021.102386.
[34] N.L. Calvo, M. Antonio, N.M. Balzaretti, T.S. Kaufman, R.M. Maggio, Chemometrics-assisted study of the interconversion between the crystalline forms of nimodipine, J. Pharm. Biomed. Anal. 158 (2018) 461–470, https://doi.org/10.1016/j.jpba.2018.06.019.
[35] D.M. Salazar-Rojas, T.S. Kaufman, R.M. Maggio, A study of the heat-mediated phase transformations of praziquantel hydrates. evaluation of their impact on the dissolution rate, Heliyon 8 (2022) e11317.
[36] R.A. Storey, I. Ymén (Eds.), Solid State Characterization of Pharmaceuticals, Blackwell Publishing, Boston, USA, 2011.
[37] N.S. Trasi, S.X.M. Boerrigter, S.R. Byrn, Investigation of the milling-induced thermal behavior of crystalline and amorphous griseofulvin, Pharm. Res. 27 (2010) 1377–1389.
[38] P. Larkin (Ed.), Infrared and Raman Spectroscopy: Principles and Spectral Interpretation 2nd Edición, Elsevier, New York, 2017.
[39] R. Chadha, J. Haneef, Near-Infrared spectroscopy: Effective tool for screening of polymorphs in pharmaceuticals, Appl. Spectrosc. Rev. 50 (2015) 565–583, https://doi.org/10.1080/05704928.2015.1044663.
[40] L.V. Ababei, A. Kriza, A.M. Musuc, C. Andronescu, E.A. Rogozea, Thermal behaviour and spectroscopic studies of complexes of some divalent transitional metals with 2-benzoyl-pyridilizonicotinoylhydrazone, J. Therm. Anal. Calorim. 101 (2010) 987–996, https://doi.org/10.1007/s10973-009-0560-z.
[41] I. Zarafu, M. Badea, G. Ionit¸a, M.C. Chifiriuc, C. Bleotu, M. Popa, P. Ionit¸a, A. Tatibouet, R, Olar. Thermal, spectral and biological characterisation of copper(II) complexes with isoniazid-based hydrazones, J. Therm. Anal. Calorim. DOI: 10.1007/s10973-018-7853-z.
[42] C.E. Miller, Near-infrared spectroscopy of synthetic polymers, Appl. Spectrosc. Rev. 26 (1991) 277–339, https://doi.org/10.1080/05704929108050883.
[43] K.T. Naveen, L.Z. Roger, C.K. Ron, T. Seema, Applications of powder X-ray diffraction in small molecule pharmaceuticals: achievements and apsiprations, J. Pharm. Sci. 107 (12) (2018) 2969–2982, https://doi.org/10.1016/j.xphs.2018.08.010.
[44] A. Shukla, E. Khan, M.H.D.B. Alsirawan, R. Mandal, P. Tandon, V.R. Vangala, Spectroscopic (FT-IR, FT-Raman, $^{13}$C SS-NMR) and quantum chemical investigations to explore the structural insights of nitrofurantoin-4-hydroxybenzoic acid cocrystal, New J. Chem. 43 (2019) 7136–7149, https://doi.org/10.1039/C8NJ05946B.
[45] X. Lu, W. Xu, M. Hanada, S.V. Jermain, R.O. Williams III, Y. Su, Solid-state NMR analysis of crystalline and amorphous indomethacin: an experimental protocol for full resonance assignments, J. Pharm. Biomed. Anal. 165 (2019) 47–55, https://doi.org/10.1016/j.jpba.2018.11.001.
[46] A. Pugliese, M. Tobyn, L.E. Hawarden, A. Abraham, F. Blanc, New development in understanding drug–polymer interactions in pharmaceutical amorphous solid dispersions from solid-state nuclear magnetic resonance, Mol. Pharmaceut. 19 (2022) 3685–3699, https://doi.org/10.1021/acs.molpharmaceut.2c00479.
[47] K. Gottschling, L. Stegbauer, G. Savasci, N.A. Prisco, Z.J. Berkson, C. Ochsenfeld, B.F. Chmelka, B.V. Lotsch, Molecular insights into carbon dioxide sorption in hydrazone-based covalent organic frameworks with tertiary amine moieties, Chem. Mater. 31 (2019) 1946–1955, https://doi.org/10.1021/ACS.CHEMMATER.8B04643.
[48] L. Mazur, K.N. Jarzembska, R. Kamiński, K. Woźniak, E. Pindelska, M. Zielińska-Pisklak, Substituent and solvent effects on intermolecular interactions in crystals of *N* -acylhydrazone derivatives: Single-crystal X-ray, solid-state NMR, and computational studies, Cryst. Growth Des. 14 (2014) 2263–2281, https://doi.org/10.1021/CG401866X.
[49] X.-S. Luo, H.-L. Deng, S. Chi, Y. Liu, M.-H. Huang, $^{15}$N Solid-state NMR as bright eyes to see the isomerization of the azo bond: revision of tris(β-hydroxyl-azo)-benzene to tris(β-ketohydrazo)-cyclohexane in porous organic polymers, J. Phys. Chem. Lett. 12 (2021) 6767–6772, https://doi.org/10.1021/acs.jpclett.1c01750.
[50] A. Lyčka, $^{15}$N NMR study of (E)- and (Z)-2-(2-(2-hydroxy-4-nitrophenyl) hydrazono)-1- phenylbutane-1,3-diones. A suitable method for analysis of hydrazone isomers, Dyes Pigm. 150 (2018) 181–184, https://doi.org/10.1016/j.dyepig.2017.10.023.
[51] M. Li, W. Xu, Y. Su, Solid-state NMR spectroscopy in pharmaceutical sciences, Trends Anal. Chem. 135 (2021) 116152, https://doi.org/10.1016/j.trac.2020.116152.
[52] N.-A. Geng, J.-M. Chen, Z.-J. Li, L. Jiang, T.-B. Lu, Approach of cocrystallization to improve the solubility and photostability of tranilast, Cryst. Growth Des. 13 (2013) 3546–3553, https://doi.org/10.1021/cg400518w.
[53] J.C. Chaumeil, Micronization: a method of improving the bioavailability of poorly soluble drugs, Meth. Find. Exp. Clin. Pharmacol. 20 (1998) 211–216.
[54] Y. Yunxia, N. Huihui, X. Shiying, G. Yingwa, W. Xiangxiang, Solubility and dissolution rate of progesterone cocrystals using 4-fluorobenzoic acid and 2-hydroxy-6-naphthoic acid as coformers, J. Cryst. Growth 585 (2022) 126601, https://doi.org/10.1016/j.jcrysgro.2022.126601.
[55] L.H. Nielsen, S. Gordon, R. Holm, A. Selen, T. Rades, A. Müllertz, Preparation of an amorphous sodium furosemide salt improves solubility and dissolution rate and leads to a faster Tmax after oral dosing to rats, Eur. J. Pharm. Biopharm. 85 (2013) 942–951, https://doi.org/10.1016/j.ejpb.2013.09.002.
[56] M. Pudipeddi, A.T.M. Serajuddin, Trends in solubility of polymorphs, J. Pharm. Sci. 94 (2005) 929–939, https://doi.org/10.1002/jps.20302.
[57] A. Veseli, S. Žakelj, A. Kristl, A review of methods for solubility determination in biopharmaceutical drug characterisation, Drug Dev. Ind. Pharm. 45 (2019) 1717–1724, https://doi.org/10.1080/03639045.2019.1665062.
[58] J. Park, H.J. Park, W. Cho, K.-H. Cha, Y.-S. Kang, S.-J. Hwang, Preparation and pharmaceutical characterization of amorphous cefdinir using spray-drying and SAS-process, Int. J. Pharm. 396 (2010) 239–245.
[59] M. Bartolomei, A. Rodomonte, E. Antoniella, G. Minelli, P. Bertocchi, Hydrate modifications of the non-steroidal anti-inflammatory drug diclofenac sodium: Solid-state characterisation of a trihydrate form, J. Pharm. Biomed. Anal. 45 (2007) 443–449, https://doi.org/10.1016/j.jpba.2007.07.002.
[60] W. Du, Y. Zhou, Y. Gong, C. Zhao, Investigation of physicochemical properties and in-vitro in-vivo evaluation of agomelatine polymorphs, Asian J. Pharm. Sci. 8 (2013) 181–190, https://doi.org/10.1016/j.ajps.2013.07.024.
[61] D.E. Kassuha, V. Aiassa, F.P. Bruno, G. Cuadra, N.R. Sperandeo, Preparation and characterization of polymorphs of the glucocorticoid deflazacort, Pharm. Dev. Tech. 20 (2015) 401–409, https://doi.org/10.3109/10837450.2013.871033.
[62] T. Watanabe, I. Ohno, N. Wakiyama, A. Kusai, M. Senna, Stabilization of amorphous indomethacin by co-grinding in a ternary mixture, Int. J. Pharm. 241 (2002) 103–111, https://doi.org/10.1016/S0378-5173(02)00196-5.
[63] A. Hédoux, Y. Guinet, L. Paccou, F. Danède, P. Derollez, Polymorphic transformation of anhydrous caffeine upon grinding and hydrostatic pressurizing analyzed by low-frequency Raman spectroscopy, J. Pharm. Sci. 102 (2013) 162–170, https://doi.org/10.1002/JPS.23346.
[64] M. Mosharraf, C. Nyström, The effect of particle size and shape on the surface specific dissolution rate of microsized practically insoluble drugs, Int. J. Pharm. 122 (1995) 35–47, https://doi.org/10.1016/0378-5173(95)00033-F.
[65] J. Knapik-Kowalczuk, Z. Wojnarowska, M. Rams-Baron, K. Jurkiewicz, J. Cielecka-Piontek, K.L. Ngai, M. Paluch, Atorvastatin as a promising crystallization inhibitor of amorphous probucol: Dielectric studies at ambient and elevated pressure, Mol. Pharm. 14 (2017) 2670–2680, https://doi.org/10.1021/ACS.MOLPHARMACEUT.7B00152.
[66] J. Liu, H. Grohganz, K. Löbmann, T. Rades, N.-J. Hempel, Co-amorphous drug formulations in numbers: recent advances in co-amorphous drug formulations with focus on co-formability, molar ratio, preparation methods, physical stability, in vitro and in vivo performance, and new formulation strategies, Pharmaceutics 13 (2021) 389, https://doi.org/10.3390/pharmaceutics13030389.
[67] N.-J. Hempel, M.M. Knopp, J.A. Zeitler, R. Berthelsen, K. Löbmann, Microwave-induced in situ drug amorphization using a mixture of polyethylene glycol and polyvinylpyrrolidone, J. Pharm. Sci. 110 (2021) 3221–3229, https://doi.org/10.1016/j.xphs.2021.05.010.

[68] H.H.Y. Tong, A.S.F. Chow, H.M. Chan, A.H.L. Chow, Y.K.Y. Wan, I.D. Williams, F.L.Y. Shek, C.K. Chan, Process-induced phase transformation of berberine chloride hydrates, J. Pharm. Sci. 99 (2010) 1942–1954, https://doi.org/10.1002/jps.21983.

[69] A. Bogomolov, M. Hachey, Application of SIMPLISMA purity function for variable selection in multivariate regression analysis: A case study of protein secondary structure determination from infrared spectra, Chemometr. Intell. Lab. Syst. 88 (2007) 132–142, https://doi.org/10.1016/j.chemolab.2006.07.006.

[70] N.L. Calvo, R.M. Maggio, T.S. Kaufman, A dynamic thermal ATR-FTIR/chemometric approach to the analysis of polymorphic interconversions. Cimetidine as a model drug, J. Pharm. Biomed. Anal. 92 (2014) 90–97, https://doi.org/10.1016/j.jpba.2013.12.036.